Influence of composition, bonding characteristics and microstructure on the electrochemical and optical stability of AlO_xN_y thin films

J. Borges[1], C. Fonseca[2,3], N.P. Barradas[4], E. Alves[4], T. Girardeau[5], F. Paumier[5], F. Vaz[1,*], L. Marques[1]

[1]Universidade do Minho, Centro/Departamento de Física, Campus de Gualtar, 4710-057 Braga, Portugal

[2]Universidade do Porto, Faculdade de Engenharia, Departamento de Engenharia Metalúrgica e de Materiais, Rua Roberto Frias, s/n, 4200-465 Porto, Portugal

[3]SEG-CEMUC – Department of Mechanical Engineering, University of Coimbra, Portugal

[4]Instituto Superior Técnico, Universidade Técnica de Lisboa, E.N. 10, 2686-953 Sacavém, Portugal

[5]Institut Pprime - UPR 3346 CNRS-Université de Poitiers-ENSMA, Département de Physique et Mécanique des Matériaux Bât. SP2MI - Téléport 2, BP 30179 F86962 Futuroscope Chasseneuil Cedex, France

*Corresponding author: F. Vaz; fvaz@fisica.uminho.pt; Universidade do Minho, Centro/Departamento de Física, Campus de Gualtar, 4710-057 Braga, Portugal. Phone: +351253601530

Abstract

Thin films of AlO_xN_y were deposited by magnetron sputtering in a wide composition range. Different structures and morphologies were observed, depending on the composition and bonding states, which opened the possibility to tailor the properties of this oxynitride system between those of pure Al and those of nitride and oxide films. In a wide range of stoichiometries, one can report the formation of nanocomposite porous films, where Al nanoparticles are dispersed in an amorphous matrix of AlO_xN_y. The electrochemical behaviour of the films was studied in isotonic NaCl solution. It was observed that the pitting

potential characteristic of aluminium disappears with the incorporation of oxygen and nitrogen in the films, being replaced by a smooth current increase. Electrochemical impedance spectroscopy performed during 35 days showed that the corrosion resistance of the films steadily increases. The unusual optical reflectance profile of some films is maintained after immersion for several months.

Keywords: Thin films; AlO_xN_y; EIS; Corrosion; Optical stability.

1. Introduction

Aluminium (Al) is known for its low density, 2.7 $g.cm^{-3}$, which is an important characteristic to reduce the weight of specific alloys, while keeping excellent mechanical properties [1], and for giving a good response to manufacturing processes [2]. Another important feature about aluminium is its good corrosion resistance, since a nm passivating oxide (Al_2O_3) film is easily formed at its surface when exposed to air and water, providing protection to the underlying metal. This passive film displays semiconducting characteristics (n-type) with a bandgap ranging from 2.5 to 4.5 eV [3]. Although the passive layer is very stable, it can undergo corrosion in more aggressive environments such as chloride (Cl^-) solutions, which can promote the so-called pitting corrosion [4]. When an improved corrosion resistance is required, anodization is often used [3, 5, 6], but the growth of AlN_x films by magnetron sputtering [7] and ion implantation [8] have also been successfully used, namely to increase the pitting potential [8]. Furthermore, it has been shown that nano and microcrystallization of aluminium can enhance its oxidation behaviour and decrease the susceptibility to pitting corrosion [9-11]. On the other hand, the electrical and optical properties of aluminium make it important in many areas of technology. It is widely used as electrical conductor in microelectronic applications [12], as electrode in some devices such as

in diodes [13, 14] and metal-insulator-metal (MIM) capacitors [15]. Most importantly, in the last years, the possibility of using Al in very/ultra large scale integration (VLSI/ULSI) technology has been studied [16, 17]. Aluminium is the preferred material to fabricate mirrors and it is also used in other optical coatings such as in surface plasmon-coupled emission (SPCE) devices [18], and it is a good candidate to be used as nonresonant plasmonic nanoparticle in thin-film silicon solar cells [19, 20]. The possibility of producing a material that combines the advantages of Al with the noblest characteristics of Al_2O_3 [3, 21-23] and AlN_x [7, 24-26], by adding small amounts of oxygen and nitrogen to Al films, leads to the development of a ternary AlO_xN_y system with tuneable properties and thus opens a wide field of applications, as also demonstrated in other oxynitride (MeO_xN_y) systems [27-33].

In previous works about the AlO_xN_y system [34-38], the authors showed that by increasing the concentration of oxygen and nitrogen in the films it is possible to obtain different microstructural characteristics, which induced a wide range of electrical and optical responses, and hence making those films potentially useful in many technological areas, such as in temperature sensors [39], medical devices such as electrode in (bio)sensors [40, 41] and in concentrated solar power (CSP) systems [42, 43]. Nevertheless, the films have to display a set of functional properties that ensures their utilization in diverse environments, namely in what concerns the contact with a particular electrochemical environment, such as the case of the human contact or simple exposure to humidity. In order to be able to draw some conclusions about the possible use of such a system in any application that may involve fluids (mostly sweat) or other type of aqueous solutions, a systematic electrochemical analysis was carried out, using one of the most common solutions tested in films containing aluminium: isotonic NaCl [4, 7]. Therefore, a set of AlO_xN_y films covering a wide range of compositions was prepared and the influence of the immersion in isotonic NaCl assessed in terms of corrosion resistance and optical properties.

2. Experimental details

2.1. Production and characterization of the thin films

The thin films were produced by reactive DC magnetron sputtering, in a laboratory-sized deposition system [36] operating at a base pressure of ~1×10^{-3} Pa, using AISI 316 L stainless steel, glass lamellae and single crystalline silicon wafers with <100> orientation as substrates, during 90 minutes. The substrates were placed in a grounded holder at 70 mm from the target, in a rotation mode-type (9 r.p.m.), and kept at a constant temperature before discharge ignition, by using a Joule effect resistor (regulated to 100 ºC and positioned at 80 mm from the substrates). Prior to the depositions, the substrates were ultrasonically cleaned and then subjected to an *in-situ* etching process, using pure argon with a partial pressure of 0.3 Pa (70 sccm), and a pulsed current of 0.6 A (T_{on}= 1536 ns and f= 200 kHz) for 900 s. A DC current density of 75 $A.m^{-2}$ was used on the aluminium target (99.6% purity) with dimensions $200\times100\times6$ mm^3, being sputtered using a gas atmosphere composed of argon (working gas), with a partial pressure fixed at 0.3 Pa (70 sccm), and a reactive gas mixture composed of nitrogen and oxygen, with a constant N_2:O_2 ratio of 17:3. Before each deposition, a target cleaning process was carried out in pure argon until the target voltage reached a steady state.

The chemical composition of the films was investigated by Rutherford Backscattering Spectrometry (RBS). Measurements were made at 2 MeV with ^{4}He and 1.4 MeV with ^{1}H, at normal incidence. There were three detectors in the chamber: one located at a 140º scattering angle respective to the beam direction, and two pin-diode detectors located symmetrically each other, both at a 165º scattering angle. The data were analyzed with the code NDF [44, 45].

The bonding characteristics were studied by X-ray Photoelectron Spectroscopy (XPS). The experiments were carried out using a Isa-Riber setup, equipped with a Mac 2 detector of

0.5 eV resolution. The pressure in the analytical chamber was kept below 10^{-8} Pa. For XPS spectra, a Mg anode was used as operating source (hν= 1253.6). For each sample, a survey scan was performed, followed by a core level spectrum of the Al-2p, O-1s and N-1s region. The binding energies were determined with respect to the C-1s peak at 284.6 eV. The XPS spectra were processed by XPSPEAK41 software.

The structure and the phase distribution of the coatings were analyzed by X-ray diffraction (XRD), using a PANalytical X'Pert PRO – MPD. The XRD patterns were deconvoluted, assuming to be Pearson VII functions to yield the peak position, peak intensity and integral breadth, using Winfit software [46].

Morphological features of the samples were probed by scanning electron microscopy (SEM), using both plane view micrographs and cross-section observations, and the chemical characterization of the samples' surface was carried out by energy dispersive X-ray spectroscopy (EDS). The SEM / EDS analysis was performed using a High resolution (Schottky) Environmental Scanning Electron Microscope with X-Ray Microanalysis and Electron Backscattered Diffraction analysis: Quanta 400 FEG ESEM / EDAX Genesis X4M, operating at 15 keV. The thickness of the samples was estimated by cross-section SEM analysis and the growth rate was calculated by the ratio between the average thickness and the deposition time (90 minutes for all samples).

Transmission Electron Microscopy (TEM) observations were performed on a JEOL 2200-FS operating at 200 kV and equipped with a field-emission gun and an energy-filter (omega). Cross-sectional specimens were investigated in bright-field, dark-field, high-resolution and selected area diffraction modes.

The electrical resistivity of the films was measured at room temperature, using the Van Der Pauw method [47] for lower resistivity values ($< 10^5$ Ω.m, using a HMS 5300 Ecopia setup) and by I-V curves, between Al contacts, for higher resistivity values.

2.2. Electrochemical characterization

AISI 316 L stainless steel specimens coated with AlO_xN_y films were cleaned by ultrasonication in isopropanol (10 minutes) and water (10 minutes). The bulk aluminium samples (99.99%) were abraded with emery paper (1000 grit) and ultrasonically cleaned in water for 10 minutes. All electrochemical experiments were performed in an isotonic sodium chloride solution (0.9% NaCl, ACS grade ≥ 99%), at room temperature. Cyclic voltammetry (CV) curves were performed at sweep rates varying from 0.1 to 6 V/s, by using a Gamry G300 equipment (Gamry Instruments, USA) driven by the Gamry PHE200 software. Electrochemical impedance spectroscopy (EIS) was performed at the open circuit potential, for frequencies ranging from 20 kHz – 10 mHz, with a 7mV (rms) AC perturbation, by using the EIS300 software from Gamry. All potentials were measured against the saturated calomel electrode (SCE), with a platinum wire as counter electrode. Simulation of the experimental data was also performed with Gamry software. The immersion times varied from a few hours to 35 days.

2.3. Optical response in real conditions

In order to study the possibility to use this film system in a real part or device, namely in what concerns their chemical and structural stability, the in-service behaviour of the samples was characterized by immersion in 0.9% NaCl solution, during approximately 4 months for reflectance measurements purposes. The reflectance values were measured weekly, in glass lamellae substrates, between 250 nm and 2500 nm using a Shimadzu UV-3101 PC UV-Vis-NIR with an attached integrating sphere of 60 mm (inner diameter). With the purpose to eliminate experimental artifacts caused by the integrating sphere, two standards, a STAN-SSH High-Reflectivity Specular Reflectance Standard (from Ocean Optics) and a WS-1-SL

Spectralon White Reflectance Standard (from Labsphere), were used for reflectance measurement correction purposes.

3. Results and discussion

3.1 Composition, bonding characteristics and structure

RBS analysis revealed uniform composition across the film thickness. For lower partial pressures of reactive gas one obtained films with a concentration of oxygen+nitrogen below 5 at%, as well as electrical resistivities close to Al-bulk [48]. For intermediate partial pressures of N_2+O_2, sub-stoichiometric AlO_xN_y films were obtained with increasing x and y coefficients as well as a gradual increase of the electrical resistivity, up to four orders of magnitude higher than the Al film. These films were indexed to a transition zone (zone T) which follows the mentioned Al-rich zone (metallic zone or zone M) and precedes a zone of close-stoichiometric Al_2O_3 films (zone C), with electrical resistivities typical of insulator materials such as alumina [49]. The composition of the samples, representative of each zone previously mentioned, can be observed in Table 1, as well as the thickness of the films and their electrical resistivity.

Fig. 1 shows the evolution of the non-metallic over aluminium (C_{O+N}/C_{Al}) atomic ratio as a function of the N_2+O_2 partial pressure. An almost linear increase of the C_{O+N}/C_{Al} atomic ratio can be observed up to a value of approximately 0.8, as the partial pressure of reactive gas increases towards 4.6×10^{-2} Pa. Above this value, the C_{O+N}/C_{Al} atomic ratio rises sharply to about 1.6, as the partial pressure of reactive gas is increased to 5.6×10^{-2} Pa, which is approximately the value that one should expect when depositing alumina-like compounds.

Particularly noticeable is the evolution of the atomic ratio of each non-metallic element over aluminium, C_O/C_{Al} and C_N/C_{Al}, which is shown in the inset in Fig. 1. It is clear that despite the large excess of nitrogen in the gas mixture (85 % N_2 + 15 % O_2), the oxygen

content in the films is very similar to that of nitrogen, which is the result of the well know higher reactivity of oxygen towards aluminium when compared to that of nitrogen [31, 32]. Although the reactive sputtering does not operate at thermodynamic equilibrium, the standard free Gibbs energy of formation of Al_2O_3 (-1.6×10^3 kJ.mol^{-1}) is much lower than the one of AlN (-2.9×10^2 kJ.mol^{-1}) [50], and thus the formation of films with higher content of oxygen is thermodynamically more favourable. This is, in fact, also verified for the film deposited with a N_2+O_2 partial pressure of 5.6×10^{-2} Pa, where a close-stoichiometric alumina-type material ($Al_2O_{2.9}N_{0.4}$) was obtained, although the partial pressure of N_2 is higher.

In order to follow the changes at the bonding level, within the different zones, a detailed XPS analysis was carried out. Figs. 2(a-b) show the line shapes for the aluminium, Al-2p, and nitrogen, N-1s, XPS lines.

The XPS analysis of the Al film, indexed to the zone M, revealed a peak centered around a binding energy of 73 eV, in accordance with the binding energy value found in literature for metallic aluminium [51-53], suggesting the existence of pure aluminium in the film, as expected. It was also possible to observe a shift in the Al-2p peak, centered around a binding energy of 75 eV, which corresponds most likely either to the Al-O line in Al_2O_3, or other bonding states of Al in $Al(OH)_3$ or AlOOH [54], since the XPS analysis did not reveal the existence of peaks corresponding to Al-N bonds.

Regarding the films within the transition zone, the presence of a Al-2p peak at 73 eV is noteworthy, indicating that a metallic aluminium phase is also present in the surface of these films. Furthermore, from Fig. 2(a) one can also observe the Al plasmon-loss peak at approximately 88 eV [53] accompanying the 2p core level of Al, which gives a plasmon energy of ~15 eV, in agreement with the Al-plasmon energy found in the literature [55]. The presence of a shifted Al-2p peak, at 75 eV, in the films indexed to zone T, indicates the possibility of the existence of either Al-O or Al-N bonds, since their binding energies in

Al_2O_3 and AlN, respectively, are very close to each other [56, 57]. Anyway, the presence of Al-N bonds is demonstrated in Fig. 2(b), where one can observe the typical N-1s peak centered around 397 eV, ascribed to aluminium nitride [57]. Overlapped with this peak is another one, centered around a binding energy of 399 eV, which is normally attributed to N-O bonds in AlN according to the literature [56, 58].

At this point, and taking into account the above discussion, one can conclude that the films ascribed to zone T are expected to be composed of a mixture of phases, where pure aluminium is mixed with aluminium nitride/oxide/oxynitride. This is a sign of the transition between pure aluminium and a nitride/oxide or oxynitride phase mentioned above. The shifts are consistent with some doping of the original metallic or nitride/oxide phases, or even the development of a kind of aluminium oxynitride phase.

In the case of the film indexed to the zone C, the metallic Al-2p peak at 73 eV vanishes, since this film is expected to be composed of close-stoichiometric alumina with poor nitrogen content, in agreement with RBS results. As it can be observed, the N-1s peak corresponding to Al-N bonds vanishes too, contrarily to the N-1s peak at 399 eV, which indicates the presence of N-O bonds and confirms the formation of aluminium oxide doped with nitrogen.

These results show a progressive decrease of the metallic character of the films, since aluminium is bonding preferably with oxygen and nitrogen to form covalent Al-N and ionic Al-O bonds as their concentration increases. This fact is expected to induce a gradual change in the crystallographic order of the films, thus opening a significant number of possible responses.

In order to follow the influence of the bonding characteristics in the structure of the films, and thus understanding the different electrochemical responses that may arise, a structural characterization was also carried out. The XRD diffraction patterns are shown in Fig. 3.

The crystalline structure was found to be Al-type (ICSD collection code: 52255), with a typical <111> preferred orientation, and a clear growing amorphization with the increase of the non-metallic content in the films, in good agreement with the composition and XPS results. This type of structural arrangement is maintained in the films within zones M and T (atomic ratios, C_{O+N}/C_{Al}, up to 0.8). For higher atomic ratios, such as the close-stoichiometric alumina film ($Al_2O_{2.9}N_{0.4}$), no diffraction patterns were detected, confirming the growing amorphization of the films. Anyway, the formation of an amorphous film is somewhat expected since the samples were prepared at relatively low temperature, and both alumina and aluminium oxynitride need significantly higher temperatures to crystallize [59, 60]. A final remark is that there is no significant peak shifting of the diffraction angles corresponding to the aluminium phase, showing that the incorporation of non-metallic elements in the crystalline aluminium is not significant as the C_{O+N}/C_{Al} atomic ratio increases.

An important result that can be drawn from the overall set of results discussed above is that the films revealed a gradual transition, in terms of bonding states and structural features, between the typical characteristics of metallic Al (indexed to the zone M) and those of amorphous alumina Al_2O_3 (zone C). According to the XPS and XRD results the films indexed to this transition zone (or zone T) are composed of an oxide/nitride/oxynitride amorphous phase containing metallic aluminium, which are becoming less crystalline as the C_{O+N}/C_{Al} atomic ratio increases. These results are consistent with the formation of a nanocomposite material where Al nanoparticles are dispersed in an amorphous oxynitride matrix, as suggested by TEM observations of these films [35, 36, 38] (see Fig. 4). The Al nanoparticles form a percolating network, which makes these films (indexed to zone T) conductive and suitable to be used as electrodes (see electrical resistivity, Table 1) [36].

3.2 Electrochemical studies in NaCl solutions

3.2.1 Open circuit potential (OCP)

The open circuit potential (OCP) values of the sputtered films stabilized after ~1.5 h of immersion in isotonic NaCl.

The sputtered aluminium film reached an OCP value of about -0.75 V, close to that of bulk Al. On the other hand, the *quasi*-pure alumina film ($Al_2O_{2.9}N_{0.4}$) revealed a clearly nobler and stabler OCP of about 0.3 V, as expected from a chemically stable and insulating oxide film known for its corrosion protection properties [23]. Concerning the films indexed to the zone T, they displayed OCP values between -0.75 and -0.65 V, which can be explained taking into consideration the model proposed before for the microstructure of these films, namely the existence of a composite formed by aluminium nanoparticles embedded in an aluminium oxynitride matrix. The application of the mixed potential theory [61] to this composite predicts that the OCP in these cases will lie between the values of aluminium and those of the oxynitride phases, with the aluminium behaving as the anode.

As a major overall conclusion, this set of results shows that the OCP values of AlO_xN_y films lie between those of Al and alumina, with the values shifting to nobler values with the increase of the amount of oxygen and nitrogen in the films.

3.2.2 Potentiodynamic analysis and its correlation with the morphology of the films

Fig. 5 shows the cyclic voltammetry results of the Al film and a representative sample of an AlO_xN_y nanocomposite film. The voltammetric curves show two main types of behaviour, corresponding to (i) a *quasi*-independence of the current on the potential for all sweep rates, Fig. 5(a), and (ii) a current vs. potential dependence that becomes stronger for higher sweep rates, Fig. 5(b). Moreover, there is a notorious correlation of these two major behaviours with the zones previously identified. In fact, the first type of behaviour (I independent of V) was

observed in the Al film (indexed to zone M) and corresponds to an almost pure capacitive behaviour, where the current density (j) is mainly ascribed to the double layer charging. The second kind of behaviour, observed in the films indexed to zone T, was characterized by a capacitive behaviour for sweep rates up to 0.8 $V.s^{-1}$ and a mixed capacitive-resistive behaviour for sweep rates between 0.8 and 6 $V.s^{-1}$, with the resistive part (I vs. V proportionality) becoming progressively more important for increasing sweep rates. This is typically observed in porous materials, where the current vs. potential dependence is related with the ohmic drop within the pores [41]. At an infinite sweep rate the CV behaviour would be described by the Ohm's law. Furthermore, the currents observed in films within zone T were one order of magnitude higher than in the Al film (for the same sweep rate). Concerning the film indexed to the zone C ($Al_2O_{2.9}N_{0.4}$), it is noteworthy that it revealed a *quasi*-independence of the current on the potential for sweep rates up to 1.5 $V.s^{-1}$. Nevertheless, the current density for the same sweep rate was about three orders of magnitude lower than the Al film. The differences in the current density are mainly ascribed to changes in the capacitance of the films, as can be observed in Fig. 6, where is plotted the double layer capacitance vs. atomic ratio of C_{O+N}/C_{Al}. The double layer capacitance (C_{DL}) was computed for each film/electrolyte interface from the slope of the straight line defined by the current vs. sweep rate plot [62]. For the zone T films only the lowest sweep rates, for which a linear relationship holds (capacitive behaviour), were considered.

From the analysis of Fig. 6, it can be observed that also in terms of capacitance the films can be indexed to the same three zones. The Al film in zone M displays a double layer capacitance of ~14 $\mu F.cm^{-2}$, then a twenty-fold capacitance increase is observed on passing to zone T films (267-360 $\mu F.cm^{-2}$), followed by a steep decrease to 67 $nF.cm^{-2}$ for the double layer capacitance of the $Al_2O_{2.9}N_{0.4}$ film. The capacitance found for the zone C film is expectable for a relatively thick, compact and strongly resistive close-stoichiometric alumina

film. Furthermore, its lowest capacitance compared to the Al film, should be mainly related with the thicknesses of the respective oxides: 460 nm for the $Al_2O_{2.9}N_{0.4}$ film and a few nm for the Al native oxide film [63].

It is remarkable the twenty-fold increase of capacitance on passing from the Al film to the film with atomic ratio C_{N+O}/C_{Al} of 0.31 ($AlO_{0.14}N_{0.17}$), and the fact that all films in zone T display high capacitance values. To find an explanation for such variation one has to consider that the double layer capacitance (C_{DL}) of a passive metal/electrolyte interface has two contributions, namely the passive film capacitance and the Helmholtz layer capacitance [4]. The total capacitance of two capacitors connected in series is given by:

$$\frac{1}{C_{DL}} = \frac{d_H}{\varepsilon_0 \varepsilon_H} + \frac{d_{ox}}{\varepsilon_0 \varepsilon_{ox}} \qquad \text{Eq. 1}$$

where ε_0 is the dielectric constant of vacuum; d_H and d_{ox} are, respectively, the thicknesses of the Helmholtz layer and of the oxide (or its space charge layer); ε_H and ε_{ox} are the dielectric constants associated with the Helmholtz capacitor and the oxide. According to Eq. 1, C_{DL} will be as high as the lowest of its components. Therefore, to explain the increase of C_{DL} from the Al film towards the films indexed to zone T it is necessary to explain the raise of both capacitances when a slight increase of oxygen and nitrogen is verified (namely in sample $AlO_{0.14}N_{0.17}$). In these conditions, the most plausible hypothesis is to assume an abrupt change of the film morphology, specifically of the exposed area, although the contribution of minor changes in dielectric constant and/or oxide film thickness of the oxynitrides cannot be discarded. This assumption is supported by the SEM images displayed in Fig. 7 and also by the observed growth rate curve reported in Fig. 6, which remarkably mimics the capacitance evolution curve, and was correlated with the type of microstructure developed by the films. In fact, the films indexed to zone T revealed a columnar-to-granular microstructure separated by voids (cauliflower growth), which is known to increase the roughness and porosity [64],

contrarily to the less-voided columnar growth observed in the Al film. This radical change of the type of growth verified from Al film to zone T induced a decrease on the films' density and thus explains the shift of the growth rate [36] (see Fig. 6). Afterwards, the gradual amorphization of the films is again inducing some densification of the voided structure, as confirmed by SEM analysis, Fig. 7. The porous and rough microstructure is likely to increase the exposed area to the electrolyte and thus the shift on the capacitance from the Al film towards zone T can be attributed to the rise of the electroactive surface area, as also reported in other porous materials [41, 65-74]. For example, the electroactive area increase was already used to explain important capacitance changes by A. Norlin et al [75] for the titanium vs. titanium nitride films and Cunha et al [40] for titanium nitride thin films of different compositions. Moreover, it is also well known by the medical biosensors researchers that the very strong capacitance increase of silver, when a silver chloride film is formed, comes mostly from the increase of roughness and porosity of the electrode [76].

The aluminium oxynitride films were also studied at a low sweep rate (1 $mV.s^{-1}$), for potential values ranging from the typical immunity region of aluminium (about -1.0 V) up to ~1.0-1.5 V, well above the typical aluminium pitting potential [4, 77]. The linear sweep voltammetry (LSV) plots of the AlO_xN_y films are displayed in Fig. 8 together with a pure aluminium bulk sample for comparison.

The pure aluminium sample revealed a corrosion potential around -1.1 V, where the anodic currents began, and a passive region extending to -0. 7 V, which are typical values for aluminium bulk material [4, 11, 63, 77-80]. The sputtered Al film exhibits a noblest corrosion potential as well as a higher pitting potential than the bulk sample, showing a passive behaviour in the potential range from - 0.7 to - 0.4 V, where the gradual thickening of the Al_2O_3 protective layer is likely to occur. These results are in line with other works that

showed an improved pitting resistance of sputtered Al films, when compared to cast Al [11, 81].

As the C_{O+N}/C_{Al} atomic ratio further increases, the typical current plateau of the aluminium LSV curve gradually disappears, as well as the pitting potential, leading to a smooth current increase with the applied potential. It is significant that the AlO_xN_y films were observed by SEM after the LSV and no pitting corrosion was apparent. The improvement in pitting resistance is ascribed to the incorporation of oxygen and nitrogen in the films. Indeed, while the increase of oxygen concentration can improve the blocking characteristics of the films, the presence of nitrogen may also have contributed to the increase of the pitting resistance since, as noted in Schäfer's work [7], the pitting corrosion of aluminium nitride coated aluminium is higher than for non-coated aluminium and it increases with the C_N/C_{Al} atomic ratio.

3.2.3 Electrochemical Impedance Spectroscopy (EIS) studies

The electrochemical responses of the nanocomposite samples (zone T) and of the Al film were studied in isotonic NaCl. The Bode diagrams, measured after one hour of immersion, are shown in Fig. 9 for representative stoichiometries. The high impedance values observed show that all interfaces are passivated and the observed differences between the impedance moduli should reflect mainly the surface morphological differences among the as-deposited films. Important to notice is also the lower impedance values for frequencies above 10 Hz observed in the films indexed to zone T, which might be an important result for electrode devices, such as the case of EEG and ECG recording [40].

The electrical equivalent circuits displayed in Fig. 10 were chosen to describe the electrochemical behaviour of the AlO_xN_y films. R_e stands for the electrolyte resistance and the upper and lower branches of the parallel circuits represent the non-faradaic and faradaic

processes taking place at the interface, respectively. The capacitive element of the non-faradaic branch was represented by a constant phase element (CPE) in order to take into account the surface roughness and other surface inhomogeneities or relaxation processes [82]. In the faradaic branch, W_σ stands for the ionic diffusion through the film, whose coefficient is given by [41]:

$$\sigma = \frac{1}{\sqrt{2}\, W_\sigma} \qquad \text{Eq. 2,}$$

and R_t stands for the charge transfer resistance, related with electrochemical processes taking place at the film/electrolyte interface. It is noteworthy that initially one tried to simulate the non-faradic part of the interface with a CPE/R parallel circuit, in order to take account of hydrogen evolution, which is thermodynamically possible at the working OCP's [83]. However, it was not possible to find consistent solutions so it was assumed that the contribution from such process is negligible. This is also confirmed from the sub-μA currents displayed for such potentials, see Fig. 8.

In what concerns the Faradic branch of the circuit, the first simulations were carried out with a CPE in parallel with R_t to simulate also the capacitive component of the charge transfer process. However, the CPE value was consistently below $2\text{-}5\times10^{-6}$ $\Omega^{-1}.cm^{-2}s^{\alpha}$, with errors higher than 60%. Once this was removed, the errors associated to the Warburg component were substantially reduced while keeping the high quality of the fits. Furthermore, in some cases, the Warburg component was found to display a low impedance and it was affected by a large error. In such cases, it was removed from the circuit without affecting the quality of the fit and decreasing the errors associated with R_t, see circuit in Fig. 10(b).

The experimental results obtained in the first set of measurements ("day zero") and the results of the fit, can be observed in Fig. 9.

The EIS study was extended for 35 days in order to monitor the evolution of the films when immersed in isotonic NaCl. The same models presented in Fig. 10 were used for the simulations, also with excellent results. The typical evolution of the Bode spectra of the oxynitride system is reported in Fig. 11, for a sample indexed to the transition zone ($AlO_{0.35}N_{0.40}$). A slight increase of the impedance moduli with immersion time, particularly for frequencies below 100 mHz, was observed. On the other hand, the phase angle clearly decreases, which is assigned to an increase of the charge transfer resistance or the Warburg impedance.

The values of the simulated parameters are plotted in Fig. 12(a-d) as a function of the immersion time. One should note that the area effect described in section 3.2.2 was taken into account.

The values observed for α are lower for the oxynitride films than for aluminium. This fact may be related with the roughness/porosity increase, in line with the CV study and the SEM images. In fact, the α parameter of the CPE closely follows the trend observed in Fig. 6 from zone M to zone T, since lower α values correspond to more rough and voided films. These values stabilize with immersion time, even if the differences among the films remain. Since the α values are close to one, the CPE values must have a strong capacitive contribution. The differences in the CPE among the samples increase with immersion time, particularly for the low oxygen/nitrogen films. This could be related, hypothetically, with a higher dielectric constant of these oxynitrides due to hydration or the incorporation of ionic species in the aluminium-rich films, such as chloride, since aluminium is known to easily incorporate chloride in its oxide [4].

On the other hand, the Warburg diffusion coefficient (σ) increases with immersion time, particularly for the oxygen/nitrogen richer films. Also, the charge transfer resistance (or corrosion resistance), steadily increases with time. This may be explained by the

reconstruction of the bulk film, as demonstrated by EDS analysis in Fig. 13, promoted by some Al dissolution and strong interfacial electric fields, which are likely to improve the films barrier characteristics by promoting the reoxidation of metallic nanoparticles, resulting in densification of the film [84]. This reconstruction of the oxide layers is only clear in the films indexed to the transition zone and this fact should be related with their nanocomposite structure, which facilitates water impregnation in the film and promotes metallic nanoparticles oxidation in the bulk. Fig. 13 shows the SEM images of $AlO_{0.35}N_{0.40}$ sample, representative of zone T, before and after the EIS measurements (~35 days immersion), where it seems evident some film´s reconstruction, resulting in the formation of a thicker oxide layer in the films indexed to the zone T, and not in the Al film, as confirmed by the increase in the C_O/C_{Al} ratio.

3.3 Influence of sodium chloride solutions in the optical reflectance

The influence of stoichiometry, morphology and structural features on the optical properties of the AlO_xN_y system were also studied in order to establish the limits for practical applicability of these coatings in optical devices [35]. The samples indexed to zone M revealed metallic-like colourations, in agreement with their high content of Al. In the case of the films indexed to the zone T, the non-metallic content becomes more important and one can report dark grey opaque-like surface tones, which is most likely the result of the change of the type of growth and morphology and decreasing metallic content. The zone C is characterized by O-rich samples with stoichiometries close to alumina (Al_2O_3), and revealed interference-like colorations consistent with their semi-transparency. According to the optical reflectance measurements, the optical profiles of the films indexed to the zone T are characterized by a nearly constant optical reflectance with values as low as 5 % from 250 nm to 2500 nm. This is an important feature for possible applications in solar devices such as CSP systems [42, 43], where the solar energy is used to heat a material with high solar

selectivity in the range of the solar spectrum (between 300 and 2500 nm) [85], with the purpose of generating electricity.

To test the optical behaviour of the deposited films in environments different from air, such as in adverse atmospheric conditions or in the sea where the Cl^- concentration can be important, some representative AlO_xN_y films were immersed in isotonic NaCl during ~4 months in order to study the influence of the immersion time on the optical reflectance. The results are plotted in Fig. 14, which shows the reflectance profile of the samples studied, in the range of 290 to 2500 nm, measured in different days, as well as the reflectance of pure aluminium (for comparison) calculated using its standard optical models [55, 86].

As it can be observed, the as-deposited Al film, with a concentration ratio of non-metallic elements below 5 at.%, has reflectance values progressively lower than the ones predicted by the optical models as the wavelength decreases. The profile of the Al film is thus distinct from a polycrystalline and uncontaminated material, mainly due to the presence of lattice defects, residual doping elements and, possibly, formation of very thin oxide/nitride layers. Nevertheless, the typical interband absorption of aluminium (at ~0.8 μm) can clearly be observed. The optical profile of the Al film gradually shifts to low values as the immersion time increases, and this is due to the formation of oxide compounds at its surface which might be the result of electrochemical reactions between the film and the electrolyte.

As the non-metallic/Al atomic ratios increases, the morphology of the films with atomic ratios, C_{O+N}/C_{Al}, between 0.3 and 0.8 consists in aluminium nanoparticles embedded in an oxynitride matrix which can induce low and nearly constant values of optical reflectance. It is important to notice that immersion in the chloride solution does not affect significantly the reflectance profiles. In fact, the $AlO_{0.14}N_{0.17}$ and $AlO_{0.35}N_{0.40}$ samples maintain the approximately constant reflectance values, which are about 10% and as low as 5%,

respectively. These features reinforce the possibility of using these coating in solar applications, even in environments containing chloride solutions.

4. Conclusions

Thin films of AlO_xN_y were deposited by reactive DC magnetron sputtering, using an aluminium target and an atmosphere composed of argon and a reactive gas mixture of N_2+O_2. Varying the partial pressure of reactive gas allowed the production of a wide range of different compositions, ranging from an Al film towards a gradual increase of the x and y coefficients, as well as an abrupt transition for Al_2O_3-type films for higher pressures. The increase of non-metallic content in the films, together with the particular deposition characteristics, induced changes in the bonding characteristics, structure and morphology of the films. This allowed indexing the deposited films to different zones concerning their features. Indeed, the overall set of results suggested the formation of nanocomposite-like materials with Al nanoparticles dispersed in an AlO_xN_y matrix (zone T), whose properties lie between the typical responses of Al (zone M) and the insulator properties of Al_2O_3 (zone C). The Al-type structure found in zone M in maintained in the transition zone with a gradual loss in crystallinity, until a complete amorphization in obtained in zone C.

The voltammetry study in sodium chloride solution showed that the typical pitting potential of aluminium vanishes as the C_{O+N}/C_{Al} atomic ratio increases, being replaced by a smooth current increase up to 1.5 V. Cyclic voltammetry proved that there is a strong capacitance increase of the films on passing from zone M to zone T, associated with the enlargement of the electroactive surface area, promoted by the formation of porous structures, followed by a sharp decrease on its value due to the formation of a dense ceramic material in zone C.

The EIS technique was used to monitor the behaviour of the films during 35 days and a gradual increase of the corrosion resistance and of the Warburg coefficient were observed. This behaviour was associated with a thickening of the oxide films, particularly in zone T.

Another important result for the films ascribed to zone T is that the unusual low and flat optical reflectance profile is maintained during 4 months of immersion in isotonic NaCl, reinforcing the possibility that these films could be used in solar applications.

Acknowledgements

This research was supported by FEDER through the COMPETE Program and by the Portuguese Foundation for Science and Technology (FCT) in the framework of the Strategic Project PEST-C/FIS/UI607/2011; the project PTDC/CTM-NAN/112574/2009 and by Programa Pessoa 2010/2011, Cooperação Portugal/França, Proc.º 441.00, Project*"COLOURCLUSTER"*. J. Borges also acknowledges FCT financial support under PhD grant Nº SFRH/BD/47118/2008 (*financiado por POPH – QREN – Tipologia 4.1 – Formação Avançada, comparticipado pelo Fundo Social Europeu e por fundos nacionais do MCTES)*.

References

[1] J.C.S. Fernandes, M.G.S. Ferreira, Corrosion behaviour of tungsten-implanted aluminium in carbonate and sulphate solutions, Surface and Coatings Technology, 56 (1992) 75-79.
[2] C. Vargel, Corrosion of Aluminium, Elsevier, Amsterdam, 2004.
[3] J.C.S. Fernandes, R. Picciochi, M. Da Cunha Belo, T. Moura e Silva, M.G.S. Ferreira, I.T.E. Fonseca, Capacitance and photoelectrochemical studies for the assessment of anodic oxide films on aluminium, Electrochimica Acta, 49 (2004) 4701-4707.
[4] F.J. Martin, G.T. Cheek, W.E. O´Grady, P.M. Natishan, Impedance studies of the passive film on aluminium, Corrosion Science, 47 (2005) 3187-3201.
[5] S. Zixue, Z. Wuzong, Porous Anodic Metal Oxides, Science Foundation in China, 16 (2008) 36.
[6] G.E.J. Poinern, N. Ali, D. Fawcett, Progress in Nano-Engineered Anodic Aluminum Oxide Membrane Development, Materials, 4 (2011) 487-526.
[7] H. Schafer, H.R. Stock, Improving the corrosion protection of aluminium alloys using reactive magnetron sputtering, Corrosion Science, 47 (2005) 953-964.

[8] J.C.S. Fernandes, M.G.S. Ferreira, J.C. Soares, C.M. Jesus, C.M. Rangel, P. Skeldon, G.E. Thompson, X. Zhou, H.H. Shimizu, The behaviour of ion-implanted tungsten species during anodic oxidation of aluminium, Journal of Physics D: Applied Physics, 31 (1998) 2083.
[9] F. Wang, The effect of nanocrystallization on the selective oxidation and adhesion of Al_2O_3 scales, Oxidation of Metals, 48 (1997) 215-224.
[10] G. Meng, L. Wei, T. Zhang, Y. Shao, F. Wang, C. Dong, X. Li, Effect of microcrystallization on pitting corrosion of pure aluminium, Corrosion Science, 51 (2009) 2151-2157.
[11] B. Zhang, Y. Li, F. Wang, Electrochemical corrosion behaviour of microcrystalline aluminium in acidic solutions, Corrosion Science, 49 (2007) 2071-2082.
[12] J.M. Camacho, A.I. Oliva, Morphology and electrical resistivity of metallic nanostructures, Microelectronics Journal, 36 (2005) 555-558.
[13] Z. Wei, T.P. Chen, L. Yang, Y. Ming, Z. Sam, W.L. Zhang, S. Fung, Charging-Induced Changes in Reverse Current-Voltage Characteristics of Al/Al-Rich Al_2O_3/p-Si Diodes, IEEE Transactions on Electron Devices, 56 (2009) 2060-2064.
[14] D.E. Yildiz, S. Altindal, On the temperature dependence of series resistance and interface states in Al/SiO_2/p-Si (MIS) Schottky diodes, Microelectronic Engineering, 85 (2008) 289-294.
[15] G. Yip, J. Qiu, W.T. Ng, Z.H. Lu, Effect of metal contacts on the electrical characteristics of Al_2O_3 dielectric thin films, Applied Physics Letters, 92 (2008) 122911.
[16] N. Joshi, A.K. Debnath, D.K. Aswal, K.P. Muthe, M. Senthil Kumar, S.K. Gupta, J.V. Yakhmi, Morphology and resistivity of Al thin films grown on Si(111) by molecular beam epitaxy, Vacuum, 79 (2005) 178-185.
[17] D.K. Aswal, J. Niraj, A.K. Debnath, K.P. Muthe, S.K. Gupta, J.V. Yakhmi, V. Dominique, Morphology-dependent electric transport in textured ultrathin Al films grown on Si, Journal of Applied Physics, 98 (2005) 026103.
[18] I. Gryczynski, J. Malicka, Z. Gryczynski, K. Nowaczyk, J.R. Lakowicz, Ultraviolet Surface Plasmon-Coupled Emission Using Thin Aluminum Films, Analytical Chemistry, 76 (2004) 4076-4081.
[19] Y. Akimov, W.S. Koh, Design of Plasmonic Nanoparticles for Efficient Subwavelength Light Trapping in Thin-Film Solar Cells, Plasmonics, 6 (2011) 155-161.
[20] Y.A. Akimov, W.S. Koh, Resonant and nonresonant plasmonic nanoparticle enhancement for thin-film silicon solar cells, Nanotechnology, 21 (2010) 235201.
[21] P.C. Snijders, L.P.H. Jeurgens, W.G. Sloof, Structure of thin aluminium-oxide films determined from valence band spectra measured using XPS, Surface Science, 496 (2002) 97-109.
[22] A. Rai, D. Lee, K. Park, M.R. Zachariah, Importance of Phase Change of Aluminum in Oxidation of Aluminum Nanoparticles, The Journal of Physical Chemistry B, 108 (2004) 14793-14795.
[23] H. Kakati, A.R. Pal, H. Bailung, J. Chutia, Deposition of nanostructured crystalline and corrosion resistant alumina film on bell metal at low temperature by rf magnetron sputtering, Applied Surface Science, 255 (2009) 7403-7407.
[24] F. Vacandio, Y. Massiani, P. Gergaud, O. Thomas, Stress, porosity measurements and corrosion behaviour of AlN films deposited on steel substrates, Thin Solid Films, 359 (2000) 221-227.
[25] F. Vacandio, Y. Massiani, P. Gravier, S. Rossi, P.L. Bonora, L. Fedrizzi, Improvement of the electrochemical behaviour of AlN films produced by reactive sputtering using various under-layers, Electrochimica Acta, 46 (2001) 3827-3834.
[26] R. Gazia, P. Mandracci, F. Mussano, S. Carossa, AlNx and a-SiOx coatings with corrosion resistance properties for dental implants, Surface and Coatings Technology, 206 (2011) 1109-1115.
[27] F. Vaz, P. Cerqueira, L. Rebouta, S.M.C. Nascimento, E. Alves, P. Goudeau, J.P. Riviere, K. Pischow, J. de Rijk, Structural, optical and mechanical properties of coloured TiN_xO_y thin films, Thin Solid Films, 447-448 (2004) 449-454.
[28] S. Venkataraj, D. Severin, S.H. Mohamed, J. Ngaruiya, O. Kappertz, M. Wuttig, Towards understanding the superior properties of transition metal oxynitrides prepared by reactive DC magnetron sputtering, Thin Solid Films, 502 (2006) 228-234.
[29] M. Fenker, H. Kappl, O. Banakh, N. Martin, J.F. Pierson, Investigation of Niobium oxynitride thin films deposited by reactive magnetron sputtering, Surface and Coatings Technology, 201 (2006) 4152-4157.

[30] N.M.G. Parreira, T. Polcar, N. Martin, O. Banakh, A. Cavaleiro, Optical and Electrical Properties of W-O-N Coatings Deposited by DC Reactive Sputtering, Plasma Processes and Polymers, 4 (2007) S69-S75.
[31] P. Carvalho, J.M. Chappe, L. Cunha, S. Lanceros-Mendez, P. Alpuim, F. Vaz, E. Alves, C. Rousselot, J.P. Espinos, A.R. Gonzalez-Elipe, Influence of the chemical and electronic structure on the electrical behavior of zirconium oxynitride films, Journal of Applied Physics, 103 (2008) 104907-104915.
[32] R. Arvinte, J. Borges, R.E. Sousa, D. Munteanu, N.P. Barradas, E. Alves, F. Vaz, L. Marques, Preparation and characterization of CrNxOy thin films: The effect of composition and structural features on the electrical behavior, Applied Surface Science, 257 (2011) 9120-9124.
[33] N. Martin, O. Banakh, A.M.E. Santo, S. Springer, R. Sanjinés, J. Takadoum, F. Lévy, Correlation between processing and properties of TiOxNy thin films sputter deposited by the reactive gas pulsing technique, Applied Surface Science, 185 (2001) 123-133.
[34] J. Borges, F. Vaz, L. Marques, AlN_xO_y thin films deposited by DC reactive magnetron sputtering, Applied Surface Science, 257 (2010) 1478-1483.
[35] J. Borges, N.P. Barradas, E. Alves, M.F. Beaufort, D. Eyidi, F. Vaz, L. Marques, Influence of stoichiometry and structure on the optical properties of AlN_x O_y films, Journal of Physics D: Applied Physics, 46 (2013) 015305.
[36] J. Borges, N. Martin, N.P. Barradas, E. Alves, D. Eyidi, M.F. Beaufort, J.P. Riviere, F. Vaz, L. Marques, Electrical properties of AlN_xO_y thin films prepared by reactive magnetron sputtering, Thin Solid Films, 520 (2012) 6709-6717.
[37] J. Borges, E. Alves, F. Vaz, L. Marques, Optical properties of AlN_xO_y thin films deposited by DC magnetron sputtering, in: M.F. Costa (Ed.) International Conference on Applications of Optis and Photonics, SPIE, Braga, 2011, pp. 80010F.
[38] J. Borges, N.P. Barradas, E. Alves, N. Martin, M.F. Beaufort, S. Camelio, D. Eyidi, T. Girardeau, F. Paumier, J.P. Riviere, F. Vaz, L. Marques, Tuneable Properties of Aluminium Oxynitride Thin Films, in: F. Vaz, N. Martin, M. Fenker (Eds.) Metallic Oxynitride Thin Films by Reactive Sputtering and Related Deposition Methods: Process, Properties and Applications, Bentham Science Publishers, 2013, pp. 195-229.
[39] J.E. Sundeen, R.C. Buchanan, Thermal sensor properties of cermet resistor films on silicon substrates, Sensors and Actuators A: Physical, 90 (2001) 118-124.
[40] L.T. Cunha, P. Pedrosa, C.J. Tavares, E. Alves, F. Vaz, C. Fonseca, The role of composition, morphology and crystalline structure in the electrochemical behaviour of TiNx thin films for dry electrode sensor materials, Electrochimica Acta, 55 (2009) 59-67.
[41] P. Pedrosa, E. Alves, N.P. Barradas, P. Fiedler, J. Haueisen, F. Vaz, C. Fonseca, TiN_x coated polycarbonate for bio-electrode applications, Corrosion Science, 56 (2012) 49-57.
[42] D. Barlev, R. Vidu, P. Stroeve, Innovation in concentrated solar power, Solar Energy Materials and Solar Cells, 95 (2011) 2703-2725.
[43] P.S. Nicholas, A. Mukul, P. Peter, Design of selective coatings for solar thermal applications using sub-wavelength metal-dielectric structures, in: K.T. Benjamin (Ed.), SPIE, 2009, pp. 74100C.
[44] N.P. Barradas, C. Jeynes, R.P. Webb, Simulated annealing analysis of Rutherford backscattering data, Applied Physics Letters, 71 (1997) 291-293.
[45] N.P. Barradas, C. Jeynes, M.A. Harry, RBS/simulated annealing analysis of iron-cobalt silicides, Nuclear Instruments and Methods in Physics Research Section B: Beam Interactions with Materials and Atoms, 136-138 (1998) 1163-1167.
[46] A. Ruhm, B.P. Topeverg, H. Dosch, Supermatrix approach to polarized neutron reflectivity from arbitrary spin structures, Physical Review B, 60 (1999) 16073.
[47] L.J. Van Der Pauw, A method of measuring the resistivity and Hall coefficient on lamellae of arbitrary shape, Philips Technical Review, 20 (1958) 220-224.
[48] D.R. Lide, Handbook of Chemistry and Physics (72nd edition), 72nd edition ed., CRC Press, Boston, 1991.
[49] J. Kolodzey, E.A. Chowdhury, T.N. Adam, Q. Guohua, I. Rau, J.O. Olowolafe, J.S. Suehle, C. Yuan, Electrical conduction and dielectric breakdown in aluminum oxide insulators on silicon, IEEE Transactions on Electron Devices, 47 (2000) 121-128.

[50] N. Jacobson, Use of Tabulated Thermochemical Data for Pure Compounds, Journal of Chemical Education, 78 (2001) 814.
[51] G.E. McGuire, Schweitz.Gk, T.A. Carlson, STUDY OF CORE ELECTRON BINDING-ENERGIES IN SOME GROUP IIIA, VB, AND VIB COMPOUNDS, Inorg. Chem., 12 (1973) 2450-2453.
[52] A. Nylund, I. Olefjord, Surface analysis of oxidized aluminium. 1. Hydration of Al_2O_3 and decomposition of $Al(OH)_3$ in a vacuum as studied by ESCA, Surface and Interface Analysis, 21 (1994) 283-289.
[53] P.M.T.M.v. Attekum, J.M. Trooster, Bulk- and surface-plasmon-loss intensities in photoelectron, Auger, and electron-energy-loss spectra of Al metal, Physical Review B, 18 (1978) 3872-3883.
[54] S. Thomas, P.M.A. Sherwood, Valence band spectra of aluminum oxides, hydroxides, and oxyhydroxides interpreted by X.alpha. calculations, Analytical Chemistry, 64 (1992) 2488-2495.
[55] E.D. Palik, Handbook of Optical Constants of Solids Academic Press, San Diego, 1998.
[56] J.C. Sánchez-López, M.D. Alcalá, C. Real, A. Fernández, The use of X-ray photoelectron spectroscopy to characterize fine AlN powders submitted to mechanical attrition, Nanostructured Materials, 11 (1999) 249-257.
[57] R. Dalmau, R. Collazo, S. Mita, Z. Sitar, X-Ray Photoelectron Spectroscopy Characterization of Aluminum Nitride Surface Oxides: Thermal and Hydrothermal Evolution, Journal of Electronic Materials, 36 (2007) 414-419.
[58] P.W. Wang, J.-C. Hsu, Y.-H. Lin, H.-L. Chen, Nitrogen bonding in aluminum oxynitride films, Applied Surface Science, 256 (2010) 4211-4214.
[59] R. Cremer, M. Witthaut, D. Neuschutz, G. Erkens, T. Leyendecker, M. Feldhege, Comparative characterization of alumina coatings deposited by RF, DC and pulsed reactive magnetron sputtering, Surface and Coatings Technology, 120-121 (1999) 213-218.
[60] N.D. Corbin, Aluminum oxynitride spinel: A review, Journal of the European Ceramic Society, 5 (1989) 143-154.
[61] M.G. Fontana, N.D. Greene, Corrosion Enginnering, McGraw-Hill Book Company, 3rd ed., 1987.
[62] J. Wang, Y. Xu, X. Chen, X. Du, Electrochemical supercapacitor electrode material based on poly(3,4-ethylenedioxythiophene)/polypyrrole composite, Journal of Power Sources, 163 (2007) 1120-1125.
[63] C. Vargel, M. Jacques, M.P. Schmidt, Chapter B.1 - The Corrosion of Aluminium, in: D. Sleeman (Ed.) Corrosion of Aluminium, Elsevier, Amsterdam, 2004, pp. 81-109.
[64] S. Mahieu, D. Depla, Reactive sputter deposition of TiN layers: modelling the growth by characterization of particle fluxes towards the substrate, Journal of Physics D: Applied Physics, 42 (2009) 053002.
[65] G.S. Attard, P.N. Bartlett, Mesoporous platinum films from lyotropic liquid crystalline phases, Science, 278 (1997) 838.
[66] C.-C. Hu, K.-H. Chang, Cyclic voltammetric deposition of hydrous ruthenium oxide for electrochemical capacitors: effects of codepositing iridium oxide, Electrochimica Acta, 45 (2000) 2685-2696.
[67] P. Costamagna, M. Panizza, G. Cerisola, A. Barbucci, Effect of composition on the performance of cermet electrodes. Experimental and theoretical approach, Electrochimica Acta, 47 (2002) 1079-1089.
[68] V. Ganesh, V. Lakshminarayanan, Preparation of high surface area nickel electrodeposit using a liquid crystal template technique, Electrochimica Acta, 49 (2004) 3561-3572.
[69] D.A. Brevnov, T.S. Olson, Double-layer capacitors composed of interconnected silver particles and with a high-frequency response, Electrochimica Acta, 51 (2006) 1172-1177.
[70] F. Jia, C. Yu, Z. Ai, L. Zhang, Fabrication of Nanoporous Gold Film Electrodes with Ultrahigh Surface Area and Electrochemical Activity, Chemistry of Materials, 19 (2007) 3648-3653.
[71] R. Mysyk, E. Raymundo-Piñero, J. Pernak, F.o. Béguin, Confinement of Symmetric Tetraalkylammonium Ions in Nanoporous Carbon Electrodes of Electric Double-Layer Capacitors, The Journal of Physical Chemistry C, 113 (2009) 13443-13449.
[72] J.B. Wu, Z.G. Li, Y. Lin, Porous NiO/Ag composite film for electrochemical capacitor application, Electrochimica Acta, 56 (2011) 2116-2121.

[73] V. Ganesh, D. Latha Maheswari, S. Berchmans, Electrochemical behaviour of metal hexacyanoferrate converted to metal hydroxide films immobilized on indium tin oxide electrodes—Catalytic ability towards alcohol oxidation in alkaline medium, Electrochimica Acta, 56 (2011) 1197-1207.
[74] N. Kobayashi, H. Ogata, K.C. Park, K. Takeuchi, M. Endo, Investigation on capacitive behaviors of porous Ni electrodes for electric double layer capacitors, Electrochimica Acta, 90 (2013) 408-415.
[75] A. Norlin, J. Pan, C. Leygraf, Investigation of electrochemical behavior of stimulation/sensing materials for pacemaker electrode applications I. Pt, Ti, and TiN coated electrodes, J. Electrochem. Soc., 152 (2005) J7-J15.
[76] D. Grubbs, D.S. Worley, New technique for reducing the impedance of silver-silver chloride electrodes, Med. Biol. Eng. Comput., 21 (1983) 232-234.
[77] P. Carbonini, T. Monetta, D.B. Mitton, F. Bellucci, P. Mastronardi, B. Scatteia, Degradation behaviour of 6013-T6, 2024-T3 alloys and pure aluminium in different aqueous media, J. Appl. Electrochem., 27 (1997) 1135-1142.
[78] S.E. Frers, M.M. Stefenel, C. Mayer, T. Chierchie, AC-Impedance measurements on aluminium in chloride containing solutions and below the pitting potential, J. Appl. Electrochem., 20 (1990) 996-999.
[79] C.M.A. Brett, I.A.R. Gomes, J.P.S. Martins, Inhibition of aluminium corrosion in chloride media: an impedance study, J. Appl. Electrochem., 24 (1994) 1158-1163.
[80] Z. Szklarska-Smialowska, Pitting corrosion of aluminum, Corrosion Science, 41 (1999) 1743-1767.
[81] G.Z. Meng, L.Y. Wei, Y.W. Shao, T. Zhang, F.H. Wang, C.F. Dong, X.G. Li, High Pitting Corrosion Resistance of Pure Aluminum with Nanoscale Twins, J. Electrochem. Soc., 156 (2009) C240-C245.
[82] M. Orazem, B. Tribollet, Electrochemical Impedance Spectroscopy, John Wiley & Sons, 2008.
[83] Y. Bai, N.C. Collier, N.B. Milestone, C.H. Yang, The potential for using slags activated with near neutral salts as immobilisation matrices for nuclear wastes containing reactive metals, Journal of Nuclear Materials, 413 (2011) 183-192.
[84] S.G. Byeon, T. Yonhua, High-performance tantalum oxide capacitors fabricated by a novel reoxidation scheme, IEEE Transactions on Electron Devices 37 (1990) 972-979.
[85] C.G. Granqvist, Solar Energy Materials, Advanced Materials, 15 (2003) 1789-1803.
[86] D.Y. Smith, B. Segall, Intraband and interband processes in the infrared spectrum of metallic aluminum, Physical Review B, 34 (1986) 5191.

Tables

Table 1 – Atomic concentration of each element (Al, O and N) in the films, thickness and electrical resistivity of the samples.

Zone	Partial pressure of N_2+O_2 (Pa)	C_{Al} / at.%	C_O / at.%	C_N / at.%	Stoichiometry	Thickness / μm	Electrical resistivity / Ω.m
Zone M	1.0×10^{-2}	100	Not detected by RBS (below 5 at.%)		Al	3.1	10^{-8}
Zone T	2.4×10^{-2}	76	10	13	$AlO_{0.14}N_{0.17}$	3.7	1.6×10^{-6}
	3.5×10^{-2}	64	20	16	$AlO_{0.31}N_{0.26}$	3.2	7.1×10^{-6}
	4.0×10^{-2}	60	18	22	$AlO_{0.30}N_{0.36}$	2.3	3.8×10^{-5}
	4.6×10^{-2}	57	20	23	$AlO_{0.35}N_{0.40}$	1.9	1.8×10^{-4}
Zone C	5.6×10^{-2}	37	54	8	$Al_2O_{2.9}N_{0.4}$	0.46	10^{11}

Figure Captions

Fig. 1 – Atomic ratios, C_{O+N}/C_{Al}, C_O/C_{Al}, and C_N/C_{Al}, as a function of the reactive gas mixture (N_2+O_2) partial pressure inside the deposition chamber.

Fig. 2 – XPS spectra of representative samples of the AlO_xN_y system, corresponding to the (a) Al-2p and (b) N-1s peaks.

Fig. 3 – Evolution of the XRD patterns of representative films, as a function of the stoichiometry.

Fig. 4 – (a) Cross-sectional dark-field TEM micrograph obtained by selecting a spot given by one set off <1 1 1> aluminium reflecting planes in Al, showing the distribution of aluminium nanoparticles. The selected area electron diffraction pattern shown in (b) was obtained by probing a circular area of 1 μm diameter in the film. Intense spots, indicating crystalline phases, and faint large rings, revealing amorphous phases, were observed. The circled bright spot labelled as g2 in (b) was selected to form the dark-field image (a). Cross-sectional high resolution TEM micrograph in (c) shows Al nanoparticles dispersed in the amorphous oxynitride matrix close to the interface.

Fig. 5 – Cyclic voltammograms of the (a) Al film and (b) of a sample representative of the typical behaviour observed in the films indexed to zone T ($AlO_{0.35}N_{0.40}$). The sweep rates used varied from 0.1 to 6.0 V/s.

Fig. 6 – Capacitance (C_{DL}) of the double layer charging region and growth rate of the films, both as a function of the C_{O+N}/C_{Al} atomic ratio.

Fig. 7 – Top view (left) and cross section (right) SEM images.

Fig. 8 – Comparative voltammetric behaviour of the AlO_xN_y films at a lower sweep rate (1 $mV.s^{-1}$).

Fig. 9 – Bode diagrams for representative films of zone T and of Al film. The measurements were made after the OCP values were stable (day "zero"). The symbols correspond to the experimental results and the solid lines represent the simulated spectra.

Fig. 10 – Electrical equivalent circuits proposed for the simulation of the AlO_xN_y/NaCl interface.

Fig. 11 – Bode diagrams of the ($AlO_{0.35}N_{0.40}$) nanocomposite film, indexed to the transition zone, as a function of the immersion time.

Fig. 12 – Electrical equivalent circuit parameters obtained from the EIS simulated spectra, using the circuits of Fig. 10.

Fig. 13 – SEM images (i) and corresponding EDS profiles (ii) of sample $AlO_{0.35}N_{0.40}$, (a) as-deposited and (b) after immersion in isotonic NaCl during ~35 days and subjected to EIS.

Fig. 14 – Optical reflectance of representative AlO_xN_y films as a function of immersion time in NaCl solution.

Fig. 1

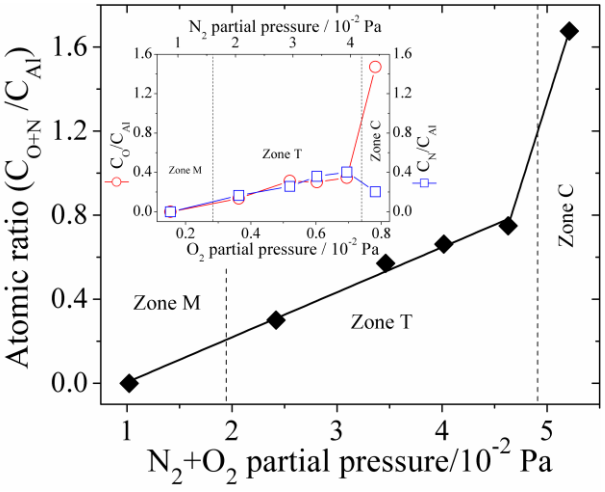
Atomic ratio (C_{O+N}/C_{Al})
N_2+O_2 partial pressure/10^{-2} Pa
Zone M
Zone T
Zone C
N_2 partial pressure / 10^{-2} Pa
O_2 partial pressure / 10^{-2} Pa
C_O/C_{Al}
C_N/C_{Al}

Fig. 2

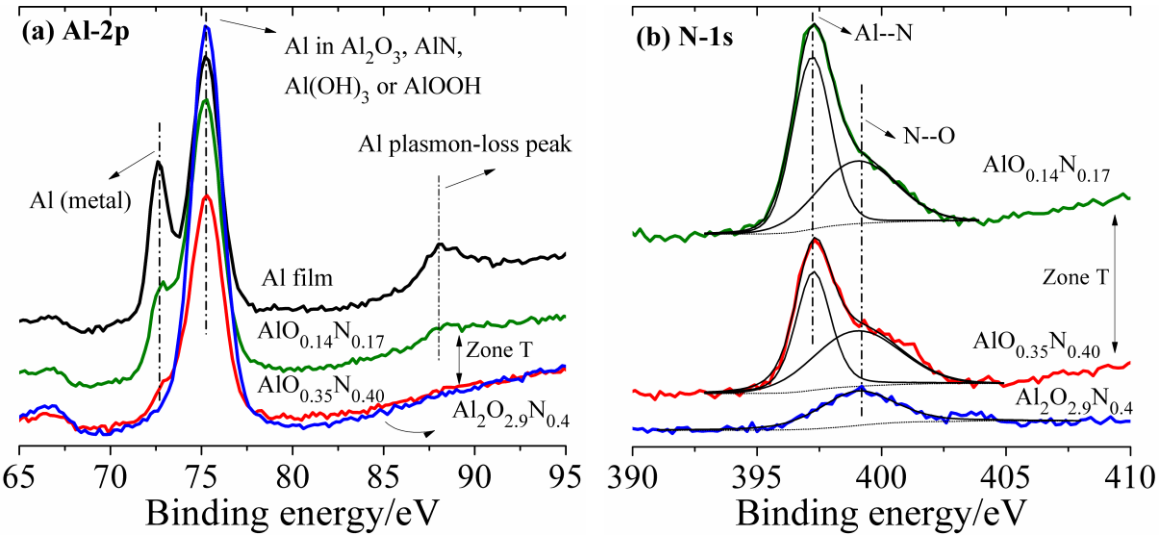
(a) Al-2p
Al in Al2O3, AlN,
Al(OH)3 or AlOOH
Al plasmon-loss peak
Al (metal)
Al film
AlO0.14N0.17
Zone T
AlO0.35N0.40
Al2O2.9N0.4
65
70
75
80
85
90
95
Binding energy/eV
(b) N-1s
Al--N
N--O
AlO0.14N0.17
Zone T
AlO0.35N0.40
Al2O2.9N0.4
390
395
400
405
410
Binding energy/eV

Fig. 3

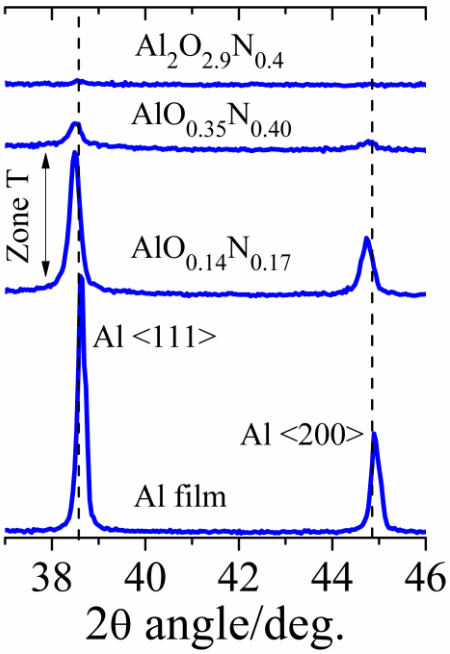
$Al_2O_{2.9}N_{0.4}$
$AlO_{0.35}N_{0.40}$
Zone T
$AlO_{0.14}N_{0.17}$
Al <111>
Al <200>
Al film
38
40
42
44
46
2θ angle/deg.

Fig. 4

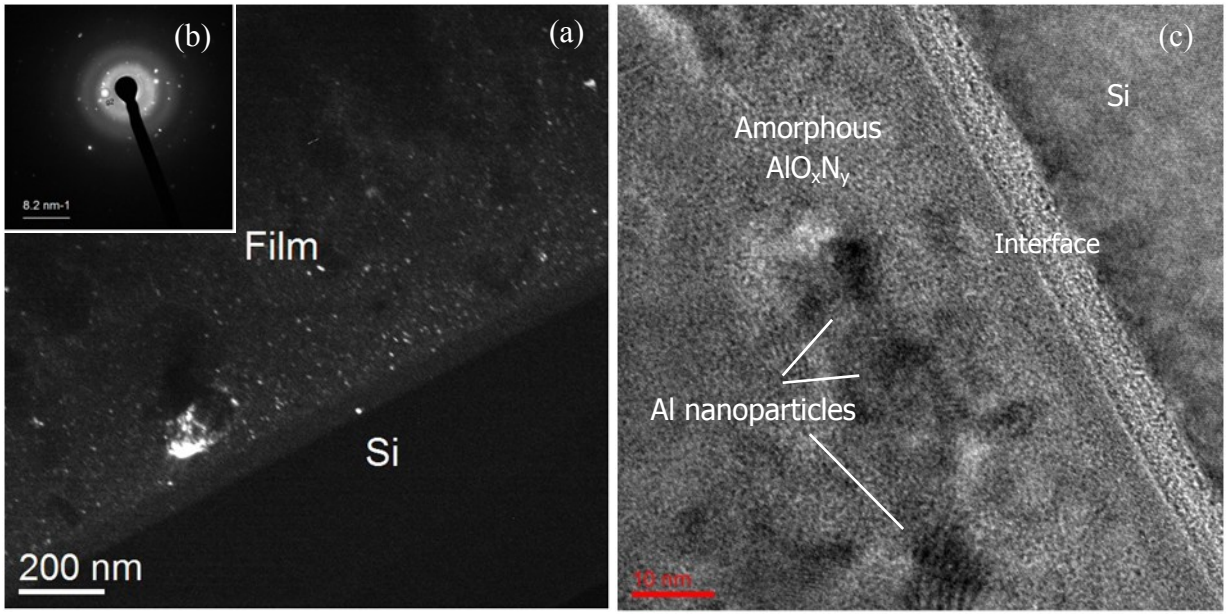
(b)
8.2 nm-1
(a)
Film
Si
200 nm
(c)
Si
Amorphous
AlO_xN_y
Interface
Al nanoparticles
10 nm

Fig. 5

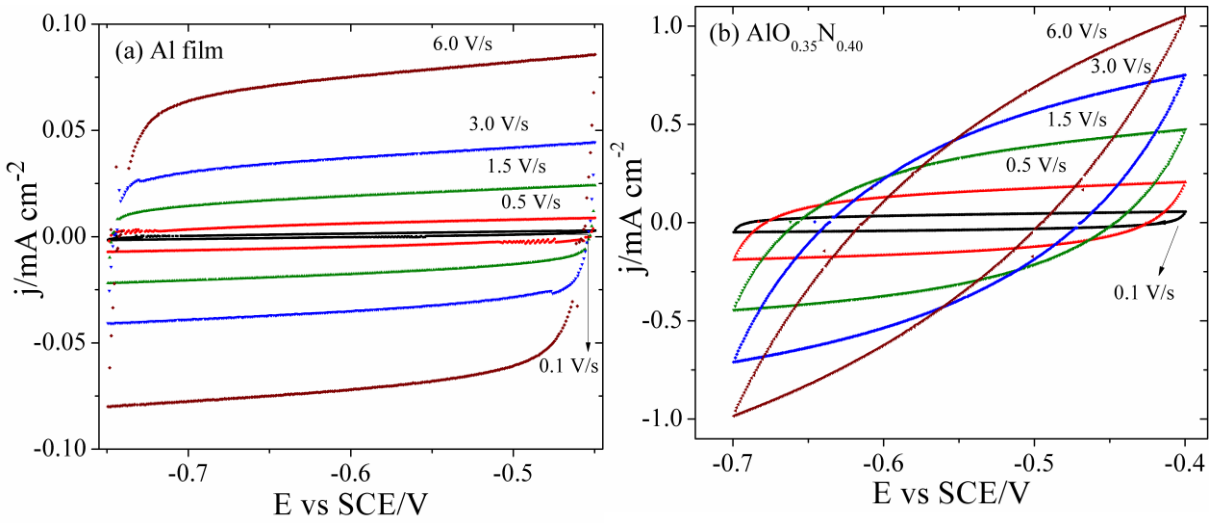
(a) Al film
6.0 V/s
3.0 V/s
1.5 V/s
0.5 V/s
0.1 V/s
j/mA cm-2
E vs SCE/V
(b) AlO0.35N0.40
6.0 V/s
3.0 V/s
1.5 V/s
0.5 V/s
0.1 V/s
j/mA cm-2
E vs SCE/V

Fig. 6

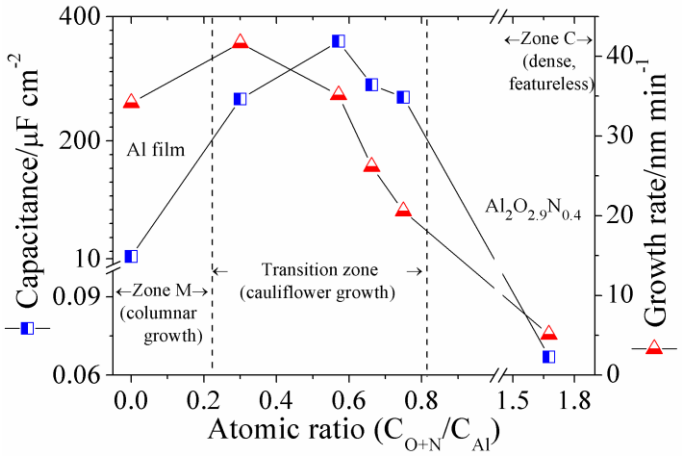
Capacitance/μF cm-2
Growth rate/nm min-1
Atomic ratio (CO+N/CAl)
Al film
Al2O2.9N0.4
←Zone M→
(columnar
growth)
Transition zone
(cauliflower growth)
←Zone C→
(dense,
featureless)
400
200
10
0.09
0.06
40
30
20
10
0
0.0
0.2
0.4
0.6
0.8
1.5
1.8

Fig. 7

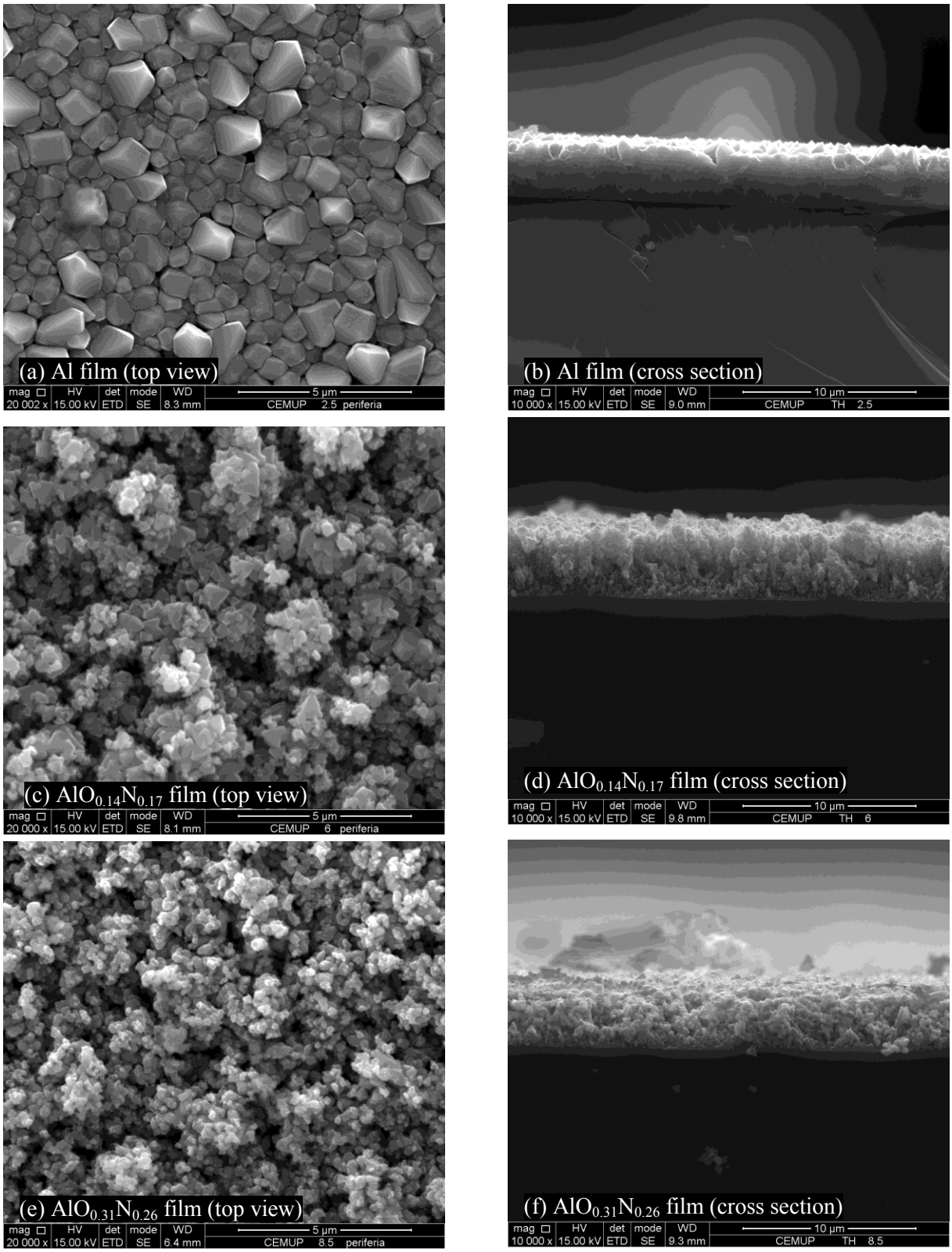
(a) Al film (top view)
mag HV det mode WD
20 002 x 15.00 kV ETD SE 8.3 mm
5 µm
CEMUP 2.5 periferia
(b) Al film (cross section)
mag HV det mode WD
10 000 x 15.00 kV ETD SE 9.0 mm
10 µm
CEMUP TH 2.5
(c) AlO0.14N0.17 film (top view)
mag HV det mode WD
20 000 x 15.00 kV ETD SE 8.1 mm
5 µm
CEMUP 6 periferia
(d) AlO0.14N0.17 film (cross section)
mag HV det mode WD
10 000 x 15.00 kV ETD SE 9.8 mm
10 µm
CEMUP TH 6
(e) AlO0.31N0.26 film (top view)
mag HV det mode WD
20 000 x 15.00 kV ETD SE 6.4 mm
5 µm
CEMUP 8.5 periferia
(f) AlO0.31N0.26 film (cross section)
mag HV det mode WD
10 000 x 15.00 kV ETD SE 9.3 mm
10 µm
CEMUP TH 8.5

Fig. 8

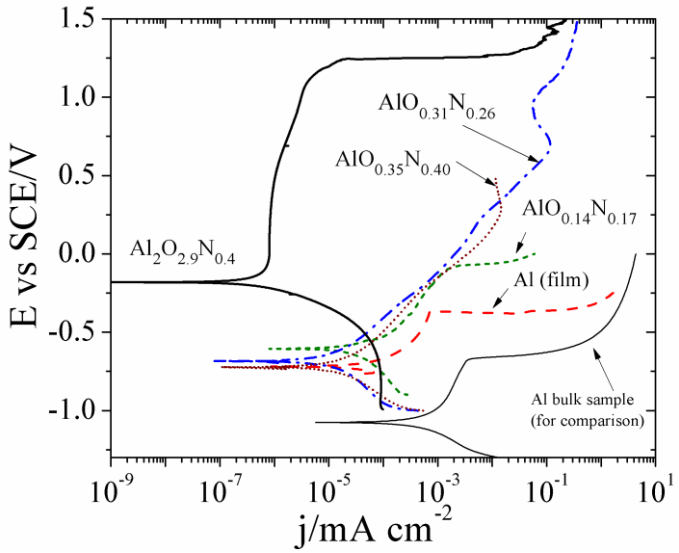
1.5
1.0
0.5
0.0
-0.5
-1.0
E vs SCE/V
10^{-9}
10^{-7}
10^{-5}
10^{-3}
10^{-1}
10^{1}
j/mA cm^{-2}
$AlO_{0.31}N_{0.26}$
$AlO_{0.35}N_{0.40}$
$AlO_{0.14}N_{0.17}$
$Al_2O_{2.9}N_{0.4}$
Al (film)
Al bulk sample
(for comparison)

Fig. 9

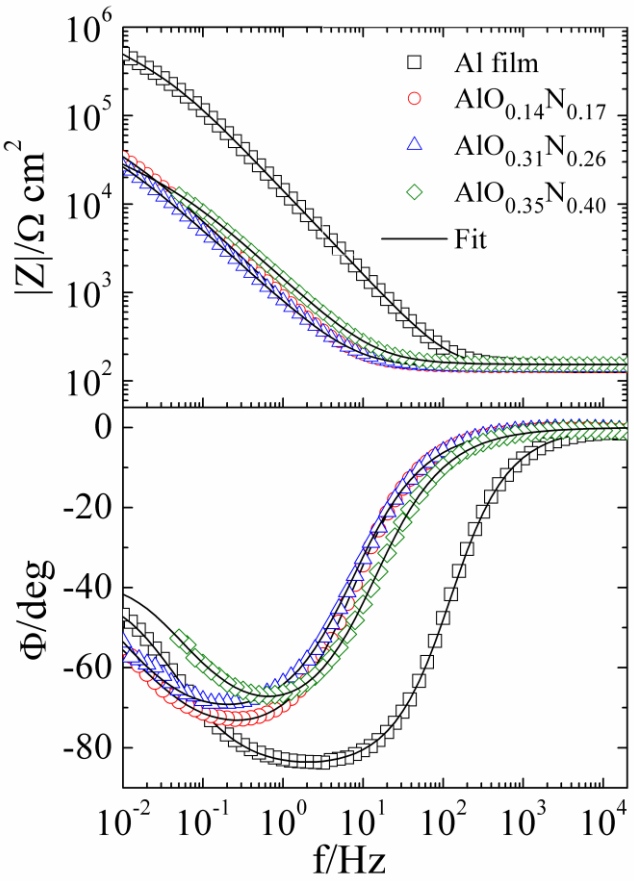
Al film
AlO0.14N0.17
AlO0.31N0.26
AlO0.35N0.40
Fit
|Z|/Ω cm2
Φ/deg
f/Hz

Fig. 10

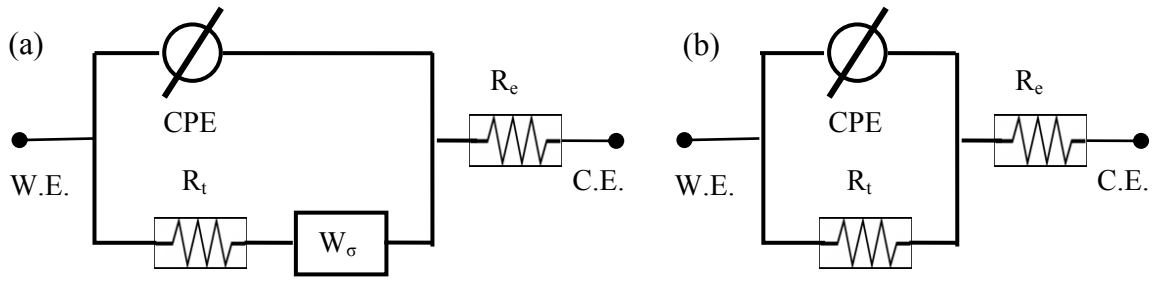

Fig. 11

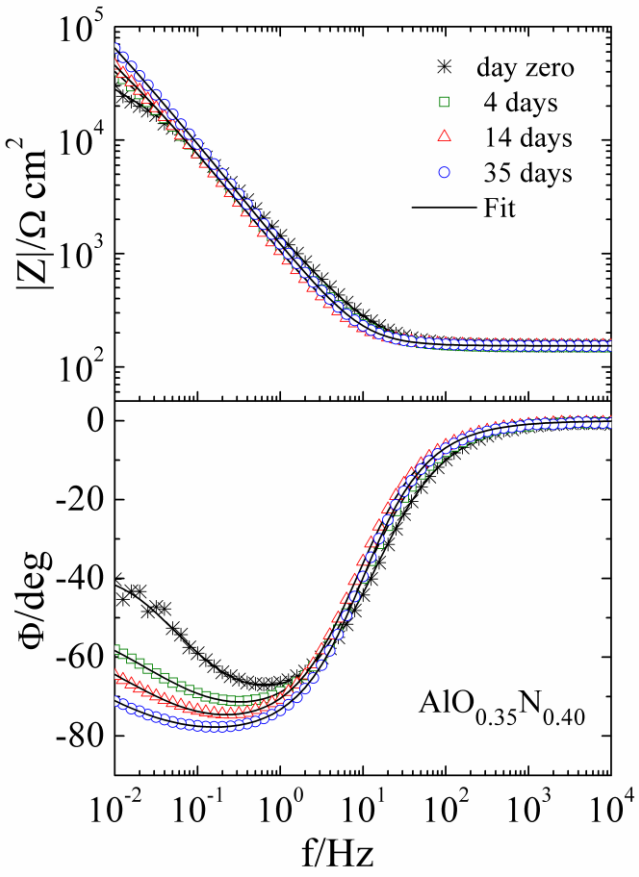

Fig. 12

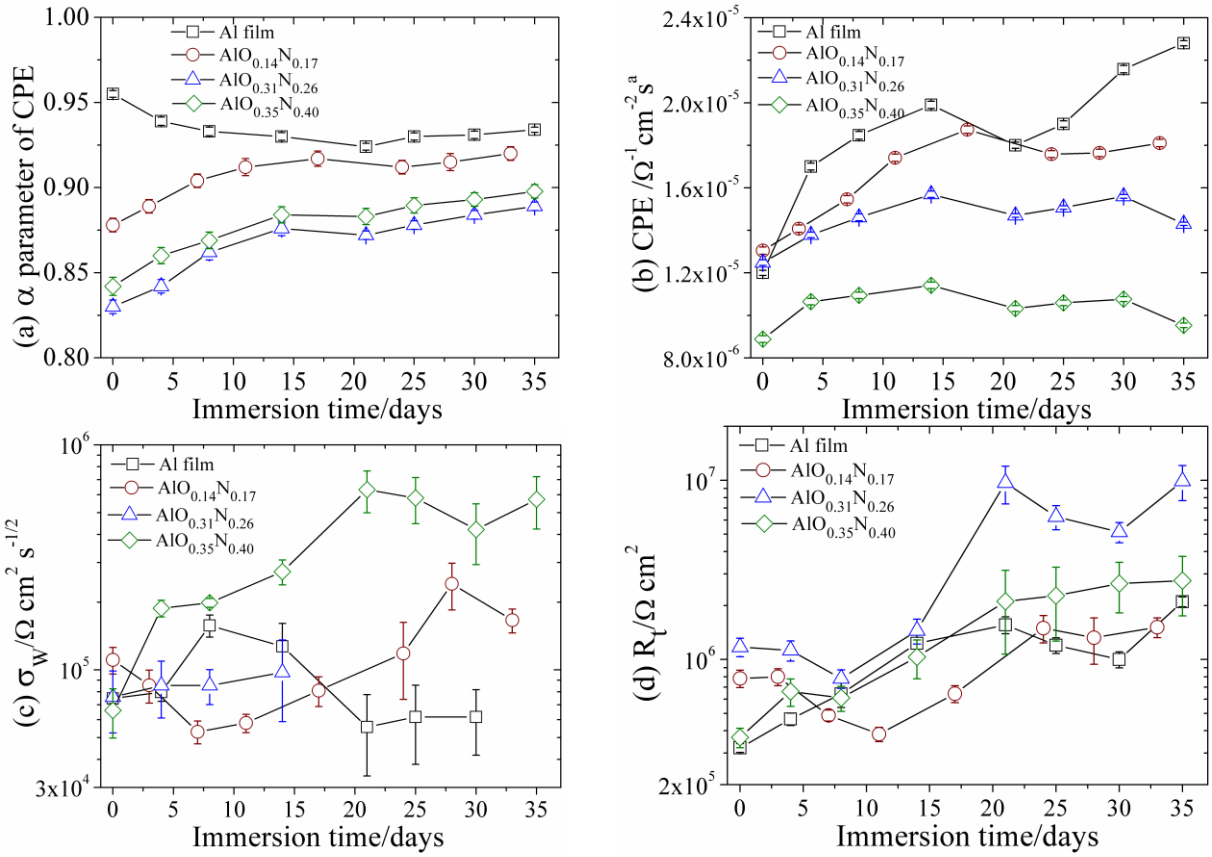
(a) α parameter of CPE
Immersion time/days
Al film
AlO0.14N0.17
AlO0.31N0.26
AlO0.35N0.40
(b) CPE /Ω-1 cm-2 sa
(c) σW/Ω cm2 s-1/2
(d) Rt/Ω cm2

Fig. 13

(a-i) $AlO_{0.35}N_{0.40}$ (as-deposited)

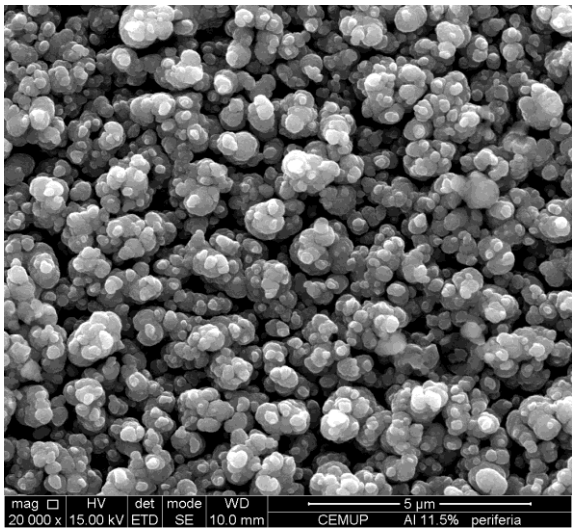

(b-i) $AlO_{0.35}N_{0.40}$ (after 35 days)

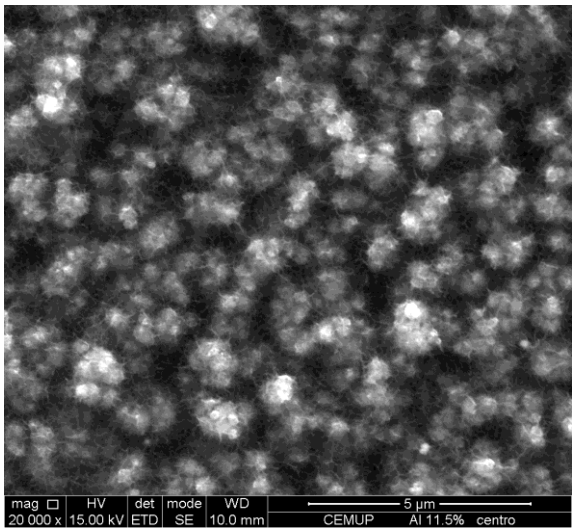

(a-ii)

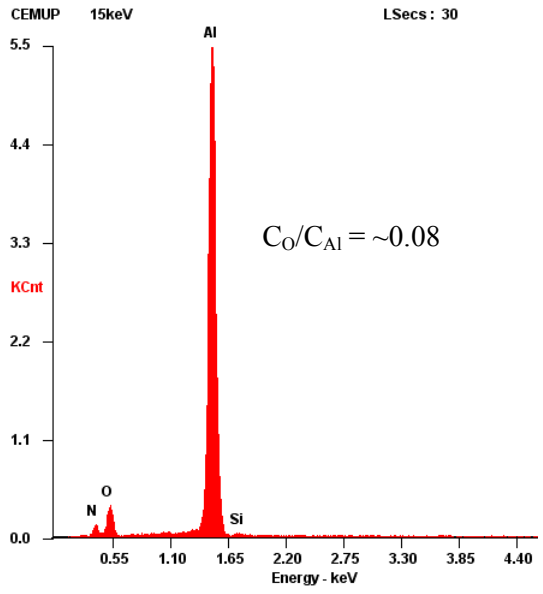

(b-ii)

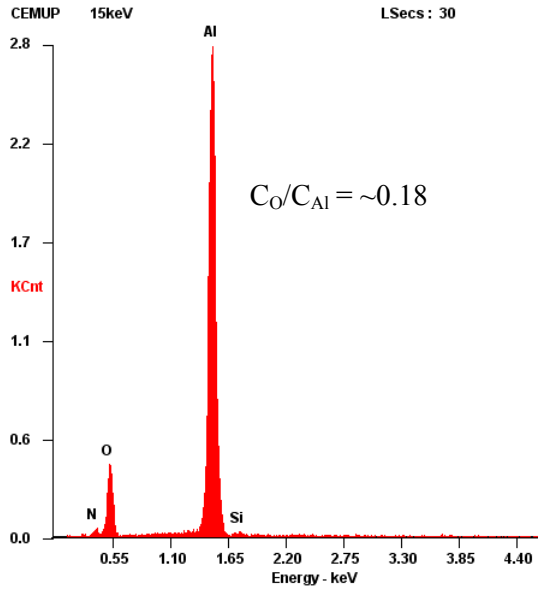

Fig. 14

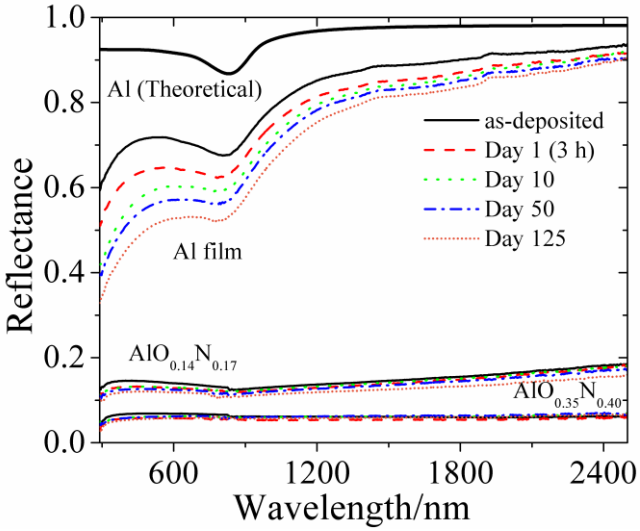
Reflectance
Wavelength/nm
1.0
0.8
0.6
0.4
0.2
0.0
600
1200
1800
2400
Al (Theoretical)
Al film
AlO0.14N0.17
AlO0.35N0.40
as-deposited
Day 1 (3 h)
Day 10
Day 50
Day 125